by R. Ludeke

# Hot-electron effects and oxide degradation in MOS structures studied with ballistic electron emission microscopy

The application of the STM-based technique of ballistic electron emission microscopy (BEEM) to the study of transport properties of SiO<sub>a</sub> gate oxide layers is reviewed. Oxide degradation observed on a local scale of nanometer dimensions ranges from the filling of electron traps with low-kinetic-energy electrons injected just above the oxide barrier, to trap generation and filling triggered by electrons with kinetic energies ≥2 eV. BEEM provides means to determine the spatial distributions of the traps. Only positively charged traps are observed for thin (≤4 nm) SiO<sub>2</sub> layers upon electrical stressing. Oxide breakdown is seldom induced by local stressing, suggesting that it occurs at extrinsic defect sites that are widely separated, BEEM also provides unique opportunities to address fundamental issues. In that regard, examples of the dynamic response of the SiO<sub>2</sub> dielectric to a moving electron are presented, as well as

the determination of the dispersion of the electron mass of the conduction-band electrons. The latter is achieved by modeling quantum interference oscillations in the BEEM current.

# 1. Introduction

With the evolution toward ever smaller devices integrated at ever larger densities, the technological challenges facing implementation of device and systems concepts and their eventual mass fabrication are rapidly leading the industry into novel territory of largely untested approaches governed by fundamental physical limits. One need only look at the SIA's National Roadmap for Semiconductors to assess the many roadblocks or potential show-stoppers that will face device integrators beyond the turn of the millennium [1]. On the device level, some of these challenges are at present limited largely by economics, such as lithography below the 0.1- $\mu$ m minimum device feature, others by a lack of suitable analytical verification

©Copyright 2000 by International Business Machines Corporation. Copying in printed form for private use is permitted without payment of royalty provided that (1) each reproduction is done without alteration and (2) the Journal reference and IBM copyright notice are included on the first page. The title and abstract, but no other portions, of this paper may be copied or distributed royalty free without further permission by computer-based and other information-service systems. Permission to republish any other portion of this paper must be obtained from the Editor.

0018-8646/00/\$5.00 © 2000 IBM

methods, such as those needed for assessing dopant distributions in future shallow-junction devices, and still others by materials issues, such as the need for low-leakage gate dielectrics. Associated with the latter, in particular, is the related issue of dielectric reliability as reflected by a current-induced degradation (electrical stressing) over time that has been observed for all metal-oxide-semiconductor (MOS) structures and devices, independently of the thickness of the dielectric [2, 3]. Progress toward addressing these challenges hinges largely on our ability to understand the associated issues from a fundamental perspective. By the very nature of the ongoing miniaturization, this perspective evolves toward a microscopic view, ultimately reaching for a description on the atomic scale.

Although integrated circuit (IC) miniaturization tends toward a two-dimensional topology dominated by interface effects, the performance-controlling properties, as well as the carrier dynamics, are still best described as bulk phenomena, albeit in a confined space of ever-shrinking dimensions that eventually will approach those associated with nanostructures (≤30 nm). Yet IC device properties are determined by materials whose properties, such as location and distributions of dopant atom and defects, must be known on a scale of a few nanometers [4]. Such precision requires analytical tools that have the needed lateral resolution, as well as sufficient subsurface sensitivity and resolution to ascertain vertical changes in material parameters. This three-dimensional capability of tools is difficult to achieve, and in practice has evolved as extensions of techniques that either require a finite material volume, such as transmission electron microscopy (TEM), or are mostly sensitive to the surface, such as the scanning tunneling microscope (STM) or atomic force microscope (AFM). This quest for analytical tools is largely exemplified by the various papers in this issue of the IBM Journal of Research and Development. In this paper we review the capabilities of probing critical properties of MOS structures at high lateral resolution with a variant of the STM-by itself an extremely surfacesensitive technique. The technique, denoted as ballistic electron emission microscopy (BEEM) [5], uses the STM tip to inject into an MOS structure electrons that are localized laterally, a fraction of which emerge in an underlying layer of the structure. A schematic representation of BEEM is shown in Figure 1. From the transmission characteristics of the injected electrons, many useful transport-related parameters of the sample can be deduced. Although referred to as a microscopy, BEEM is more frequently used in a spectroscopic mode, in which the current transmitted through the layered structure is measured as a function of the electron energy, while the STM tip remains stationary. BEEM, more frequently applied to metals in direct contact with semiconductors

[6], including semiconductor heterostructures [7], was first applied to a metal-insulator-semiconductor (MIS) structure of Au/CaF<sub>2</sub>/Si(111) [8], and shortly thereafter to MOS structures [9, 10].

The reliability of gate dielectrics is generally assessed by applying a potential across a MOS capacitor or fieldeffect transistor (MOSFET) and measuring the time or integrating the current until the structure fails [2, 3, 11, 12]. The resulting total charge  $Q_{\mathrm{RD}}$  is referred to as the charge to breakdown. This form of electrical stressing affords few opportunities for spectroscopic assessments or other forms of characterization. Such constraints can be partly overcome in stressing studies with BEEM, with the added advantage of high lateral resolution. This is possible because the STM tip is capable of injecting currents that produce high current densities ( $\sim 10^6$  A/cm<sup>2</sup>) at energies exceeding 10 eV into the metal layer of an MOS structure. Of the order of 1% of the injected electrons may be transmitted through the oxide and reach the Si substrate of the structure. This capability gives BEEM the unique ability to electrically stress the oxides on a microscopic scale and assess the resulting degradation with the same instrument operating in the spectroscopic mode at the location of the applied stress. This stress-probe approach is discussed in Section 3, following the description of BEEM applied to MOS structures. In Section 4 we discuss some novel applications of BEEM to extract fundamental oxide parameters, in particular the dynamic dielectric constant and the conduction-band mass of SiO<sub>2</sub>.

#### 2. Experimental details

#### • MOS samples for BEEM studies

The structures used in our studies consisted of metal dots evaporated in ultrahigh vacuum (UHV) onto oxidized Si wafers. The choice of the metal is critical, as it must wet and adhere to SiO, to achieve full coverages at thicknesses of less than 10 nm, and it must be able to withstand the high fields and currents of the STM at tip biases used in BEEM studies of MOS structures ( $\sim$ 3–12 V). We have found Pt, Pd, and W to be quite suitable. We used devicegrade amorphous SiO, layers that were thermally grown in the range 750-800°C at 1 atm. of dry oxygen for 30-50 minutes at the IBM Advanced Silicon Technology Laboratory. The substrates used were 125-200-mmdiameter Si(100) wafers doped to the low 10<sup>17</sup> cm<sup>-3</sup> range. The thicknesses of the oxide layers were in the ultrathin range of 2.3 to 7.5 nm, as measured with an ellipsometer. If the thickness was critical to the analysis, capacitance-voltage (C-V) measurements were used to corroborate the optical determinations. Samples of approximately 8 mm × 15 mm were cleaved from the wafers and introduced into an ultrahigh-vacuum (UHV) preparation chamber. Prior to metal deposition, the

518

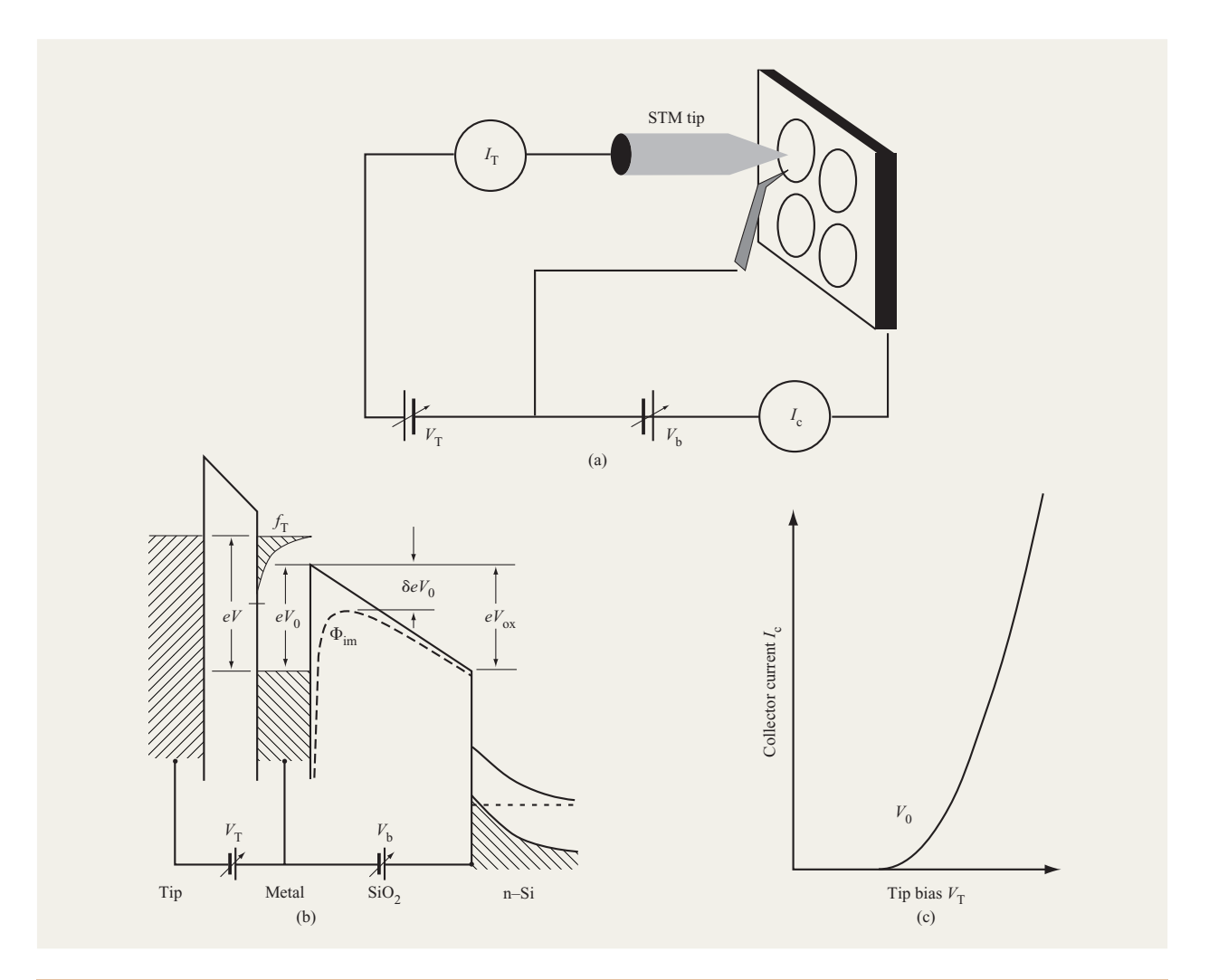
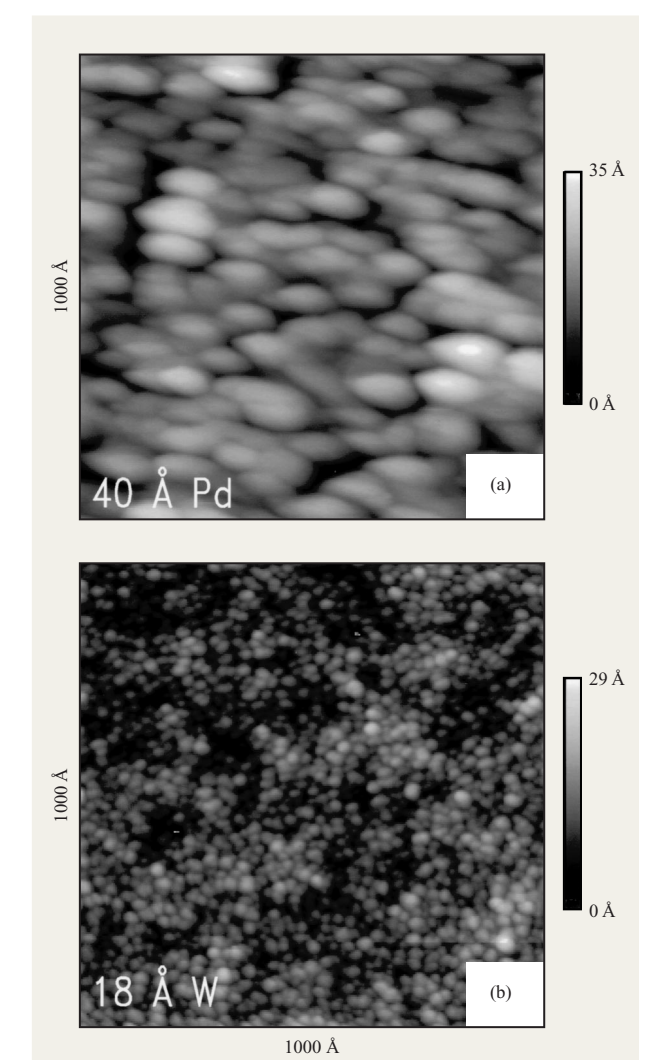


Figure 1

(a) Schematic representation of a BEEM experiment. The STM tip injects a constant tunnel current  $I_{\rm T}$  into the metal overlayer represented by one of the four circles. The STM tip bias  $V_{\rm T}$  is referenced to the metal through a movable contact. A bias potential  $V_{\rm b}$  may also be applied between the metal and the substrate. (b) Energy-band diagram for a BEEM experiment on a MOS structure for positive oxide bias  $V_{\rm ox}$ . The bias  $V_{\rm ox}$  is controlled by means of the "gate" bias  $V_{\rm b}$ . The energy distribution of the STM-injected electrons is represented by the exponential function  $f_{\rm T}$ . The energy  $eV_0$  is the energy difference between the Fermi level  $E_{\rm F}$  of the metal layer and the bottom of the SiO $_2$  conduction band in the absence of image force effects. The dashed line represents the barrier profile with image force correction included. (c)  $I_{\rm c}$  vs.  $V_{\rm T}$  or BEEM spectrum obeying a power-law behavior in the absence of any inelastic scattering.

samples were annealed at about 250°C for several hours to remove water and other volatile surface contaminants. Arrays of ultrathin metal dots, 0.2 mm in diameter, were deposited by thermal evaporation through a shadow mask. The substrate was cooled to about 30 K by mounting it on the cold finger of a liquid He cryostat. Deposition at low temperature inhibits surface diffusion, which results in a continuous, pinhole-free ultrathin film of a finer-grained morphology at a lower thickness than would be achieved at higher temperatures. The finished sample was allowed to warm to room temperature and was subsequently

transferred under UHV into the STM chamber. A grounding contact needed to bias the tip of the STM relative to the metal overlayer was subsequently carefully positioned onto a selected metal dot by means of three orthogonally mounted Inchworms\*\*. STM images of Pd and W deposited at 30 K are shown in Figure 2; the latter was evaporated by electron-beam heating. A smooth surface morphology is needed to minimize BEEM image contrast arising from the surface topography of the metal, which has been observed to strongly modulate the BEEM image [13].



STM images of (a) a 4-nm-thick Pd layer and (b) a 1.8-nm-thick W layer. Both were deposited onto thermally oxidized Si(100) at a substrate temperature of 30 K. From [46], with permission.

• Ballistic electron emission microscopy/spectroscopy
As mentioned earlier, BEEM is a variant of conventional STM. It differs by the requirement of a thin, generally metallic conducting layer on the substrate—the  ${\rm SiO}_2$ – ${\rm Si}$  structure in the present case—and by the need to contact the metallic film. The sole purpose of the latter is to provide a potential reference plane (generally at ground potential) relative to which the STM tip is biased. The electrons injected into this layer by the STM tip have an energy equal to  $eV_{\rm T}$ , where  $V_{\rm T}$  is the STM tip bias [Figure 1(a)]. The thickness of the metal layer is comparable to or preferably less than the electron mean free path, so that

the electrons can traverse the layer ballistically (without scattering). If their energy exceeds that of the potential step at the interface—in this case the difference  $eV_0$  between the Fermi level  $E_{\rm F}$  in the metal and the bottom of the  ${\rm SiO}_2$  conduction band—the electrons have a finite probability of being injected into the conduction band and, after traversing the oxide, reaching the Si substrate, whence they emerge as a collector current  $I_{\rm e}$ .

A band diagram for a BEEM experiment is illustrated in Figure 1(b) for the conditions of a positive (accelerating) oxide potential. The probability that the electrons reach the Si is dependent on the overlap of conduction-band density of states at the interfaces, the transmission probability  $T_{\rm ox}$  across the oxide, and transmission probabilities of a quantum-mechanical origin. In the simplest approximation, the collector current  $I_{c}$ beyond the threshold voltage  $V_0$  follows a power law, which is schematically shown in Figure 1(c). These issues have been detailed elsewhere [9]. Suffice it to say here that  $T_{ox}$  is strongly dependent on the scattering rates of electrons with longitudinal optical phonons (energydispersive) and acoustic phonons (momentum-dispersive), rates which are strongly dependent on the kinetic energy of the electrons [2, 14]. The kinetic energy in the oxide is determined by the energy at the point of injection  $(eV_{\rm T} - eV_{\rm 0})$  modified by any gain or loss in energy from field acceleration due to the presence of an oxide potential  $V_{\rm ox}$ . The latter is a combination of a built-in potential arising from work-function differences between the metal and substrate, as well as from likely oxide charges, and an externally applied bias  $V_{\rm b}$ .

In the spectroscopy mode of BEEM, the scanning of the STM is interrupted and the collector current  $I_{\rm c}$  is measured as the tip bias  $V_{\rm T}$  is ramped over a range that includes the barrier step potential  $V_{\rm 0}$ . The current  $I_{\rm c}$  becomes finite once  $V_{\rm T}$  exceeds  $V_{\rm 0}$  for  $V_{\rm ox}>0$  or exceeds  $V_{\rm 0}-V_{\rm ox}$  for  $V_{\rm ox}<0$ . The STM is generally operated at a constant tunneling current  $I_{\rm T}$  in the 0.5- to 5-nA range. The current  $I_{\rm c}$  also provides image contrast in the scanning mode, thereby generating an electron transmission image of the MOS structure, commonly referred to as a BEEM image [5], that is recorded simultaneously with the STM topographic image. Examples of BEEM images are given in Section 4.

Electrical stressing with BEEM is achieved by injecting hot electrons of energy  $eV_{\rm T}$  while the tip is either scanning over a selected area or stationary for a predetermined time at a specific location on the sample surface. The time-integrated collector current determines the total charge injected. An  $I_{\rm c}$  vs.  $V_{\rm T}$  or BEEM spectrum is taken prior to and during the experiment to assess the consequences, which may lead to changes in the local transmission characteristics, including threshold shifts  $\delta V_{\rm 0}$ . This process is then repeated until either the stressed area

moves out of range because of instrument drifts, or the oxide breaks down, as evidenced by a low value of  $V_0$ . Alternatively, spectra over a broad energy range are repeatedly taken at the same spot until either of the two previously mentioned events occurs. As a point of reference, a collector current of 50 pA collected over an area of 5 nm² (realistic for oxides dominated by ballistic transport, i.e., oxide thickness  $t_{ox} \leq 5$  nm) corresponds to a charge injection of  $10^3$  C/cm²-s! In our experiments we can achieve injection energies of 9 eV. To achieve this value by conventional Fowler–Nordheim injection, one would need to apply a field of  $\sim$ 24 MV/cm to a 5-nm-thick oxide. Larger effective energies can be achieved with BEEM by applying an accelerating oxide bias.

#### • Monte Carlo simulations

Although the BEEM current through an MOS structure can in principle be simulated by Monte Carlo solutions of the Boltzmann equation, a lack of knowledge of scattering parameters, primarily in the metal and at the metal-SiO, interface, make such an endeavor doubtful at present. However, a better knowledge of scattering processes in SiO<sub>2</sub> and Si makes feasible a partial simulation of a BEEM experiment. Details of the Monte Carlo simulations, which are based on the code developed by Fischetti et al. [11], have been discussed elsewhere [9, 15]. Here we give an example of how Monte Carlo simulations can be used to estimate the spreading of the electron beam as it traverses an SiO, layer. Knowledge of the spreading is needed in order to estimate current and injected charge densities during electrical stressing of the layer, as well as to assess the thickness and energy range for which electron wave interference may be expected, a topic that is discussed in Section 4. In order to calculate the spreading of the beam in the oxide layer, we assume that the electrons reach the metal-SiO2 interface at normal incidence (this precludes appreciable scattering in the metal, a reasonable assumption for the ultrathin metal films used). The potential in the oxide includes image force corrections and an applied oxide bias, a topic to be discussed further in Section 4. We also assume that electrons returning to the metal can be neglected. The spreading is then obtained as follows: First the position of the transmitted electrons is recorded, and the normalized local current density,  $j(r)/I_{in}$ , is calculated after sufficient statistics have been acquired (typically 10<sup>5</sup> electrons). The distance r is measured with respect to an origin at the injection point;  $I_{in}$  is the injection current. Typical results of associated simulations are summarized in Figure 3 for different combinations of oxide thickness, oxide bias, and tip bias. The two distributions for  $V_{\rm T} = 5.5$  (open symbols) were obtained at a small accelerating bias. At this value of  $V_{\rm T}$ , the electrons travel at an energy of 1.5 eV through the oxide, where phonon scattering is

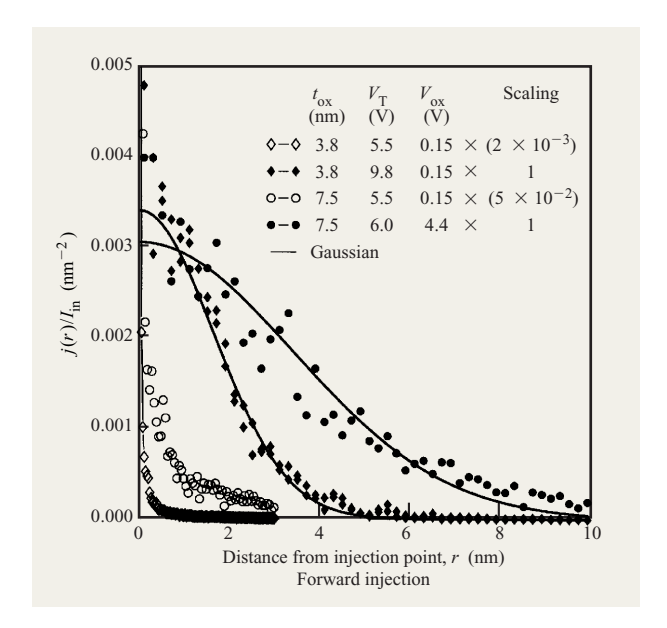
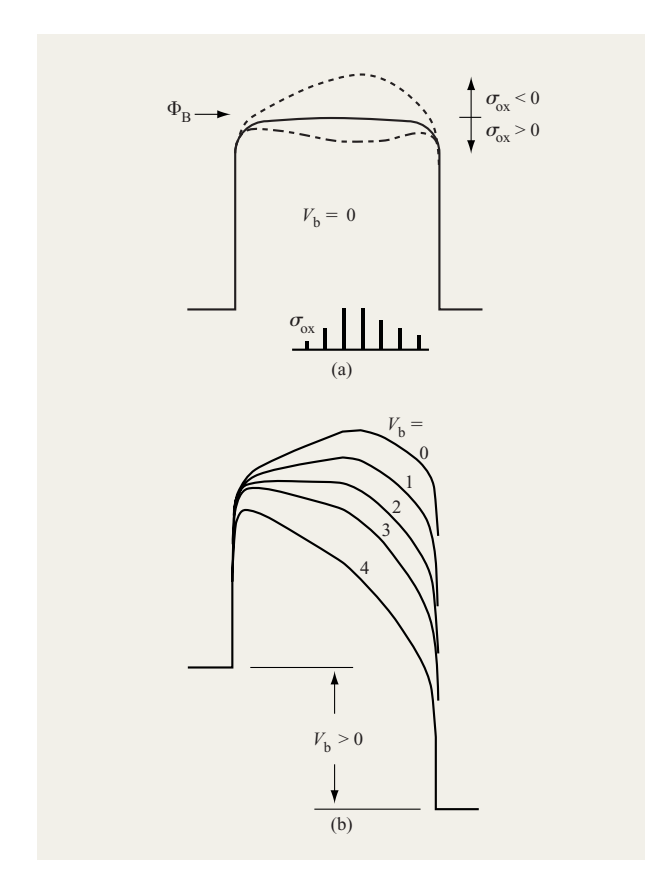


#### Figure 3

Spatial distribution of the normalized current densities at the Si/SiO $_2$  interface after electron transport through 3.8- and 7.5-nm-thick SiO $_2$  films, as calculated by Monte Carlo simulations for various bias conditions. The figure serves to illustrate the strong dependence of the beam spreading on the electron energy in the oxide. At relatively low electron energies (open symbols,  $V_{\rm T}=5.5$  V), little broadening is predicted. Strong broadening due to electron-acoustic phonon scattering occurs if electrons are either injected at high energy (3.8 nm,  $V_{\rm T}=9.8$  V, solid diamonds), or if the electrons are heated inside the oxide by a strong electric field (7.5 nm,  $V_{\rm ox}=4.4$  V, solid dots). From [15], with permission.

small and mostly via longitudinal optical phonons (forward scattering). This results in a streaming-type motion in the presence of a small accelerating field and leads to very little beam broadening. In this case the beam size on the substrate side is expected to be comparable to the size of the injection beam. The two distributions were scaled to the same heights in such a way that the additional broadening in the thicker oxide could be clearly seen. The peak at r=0 overshoots the y-axis of the plot by one order of magnitude, indicating that the broadening is considerably smaller than is suggested at first glance.

Considerably broader distributions are obtained if the electrons are either accelerated by a strong electric field (7.5-nm-thick film, solid circles) in the oxide or injected at high energies (3.8-nm-thick film, solid diamonds). The broadening is caused by a rapid increase of the acoustic phonon scattering (isotropic and quasi-elastic [14]) with increasing kinetic energy of the electrons. This scattering dominates at kinetic energies above 2 eV and leads to strong backscattering that both reduces the transmission



Model calculation of the effect of a distributed charge in the oxide on the barrier profile. (a) For flatband conditions, a negative charge raises the potential; an equal but positive charge has an opposite but diminished effect. Image force effects arising from both metal and Si substrate have been included. (b) Field dependence of the potential barrier for a negative charge ( $\sigma_{\rm ox}=1.6\times10^{13}/{\rm cm^2}$ ) distributed as shown in the middle of the figure.

probability and significantly spreads the beam. In the case of the 3.8-nm-thick film, the electrons were injected at a tip bias of 9.8 V, which corresponds to an initial electron energy in the oxide of about 5.8 eV. Alternatively, electrons were injected at an energy of 1.5 eV into a 7.5-nm-thick oxide and subsequently heated by a strong electric field, such that their average energy reached values of 4–5 eV. Again, significant beam spreading is predicted, and the increased oxide thickness leads to additional broadening. Under conditions in which the electrons reach energies in excess of 3–4 eV, the beam size on the substrate side is largely determined by acoustic phonon scattering in the oxide. This beam spreading is later used to estimate local current densities and charge densities at breakdown.

# 3. Charge trapping and oxide degradation

Injection of hot carriers into SiO, gate oxide layers is known to produce charges in the oxide by trapping electrons and holes [2, 16], a process that ultimately leads to failure. The present understanding of degradation and breakdown mechanisms is largely based on studies on MOS capacitor structures with techniques such as Fowler-Nordheim (F-N) tunneling and internal photoemission [2, 11, 14, 17-25]. The results of these studies represent properties averaged over areas of  $\sim 10^{-4}$ to 10<sup>-2</sup> cm<sup>2</sup> that do not include the effects of sample inhomogeneities on a microscopic scale. A further shortcoming of the standard injection methods is the need for high fields (of order  $10^7$  V/cm) to energize the electrons, which exhibit a position-dependent energy as they traverse the oxide. For oxides exceeding ~10 nm in thickness, the kinetic energy of the electrons in such fields may reach values sufficient to cause impact ionization in the oxide [2, 14, 17, 18]. Even at much lower fields, the electron may impact-ionize holes in the Si with energies (>5 eV) sufficient to cause them to be injected back into the valence band of the SiO<sub>2</sub>, resulting in oxide damage [11, 16]. The presence of hot carriers of both polarities and diverse energies complicates the determination of oxide-degradation mechanisms. The two most discussed mechanisms, referred to as impact ionization and trap creation, are premised on the strong electron heating in high-field transport across the oxide [2, 11, 14, 17–19]. Impact ionization in the SiO<sub>2</sub>, or electron-hole pair creation, occurs when electrons exceed the bandgap energy of 9 eV. In the trap-creation process, defects are generated by hot electrons breaking hydrogen-silicon bonds near the anode. The released hydrogen atoms or ions rapidly diffuse to the cathode, where they combine with other hydrogen atoms, thereby creating additional defects. This model assumes a soft threshold energy of ~2 eV needed to break the Si-H bonds [2, 26].

In this section we cover observations with BEEM of the existence of both negative and positive charge in the oxide. Negative charge is generally observed only in oxides having thicknesses of ~4 nm and above, whereas positive charge is observed for oxides of thickness below 4 nm. The reason for this behavior is attributed to detrapping of the negative charge that resides in levels of sufficiently high energy in the SiO<sub>2</sub> bandgap to be able to tunnel into empty states in either the metal or the Si substrate. The principal effect of the presence of oxide charge on a BEEM spectrum is a shift of the threshold energy, which is a direct measure of the net barrier height. This point is illustrated in part (a) of Figure 4 for a model calculation of the oxide potential for a charge distribution represented by the bar graph shown in the figure [27]. The effect of a negative charge is more pronounced in altering the threshold voltage  $V_0$  in the BEEM spectrum. We first

discuss the observation of negative charge in thicker oxides, which has two components: One arises from traps that existed before the stressing, the other from traps generated during injection by hot electrons of energy  $\geq 2$  eV relative to the bottom of the SiO<sub>2</sub> conduction band. The distributions of both types of traps across the oxide are determined. In the following section we discuss the observation of positive charge.

• Electron traps: Energetics and distributions in thicker oxides. The observation has frequently been made that repeated measurements on the same location of an MOS sample result in a shift in the threshold energy to higher energies. An example is shown in Figure 5 for a 7.1-nm-thick SiO<sub>2</sub> layer. After a few scans the shifting subsided, an indication that the filling of the traps had saturated, provided that the kinetic energy of the injected electrons

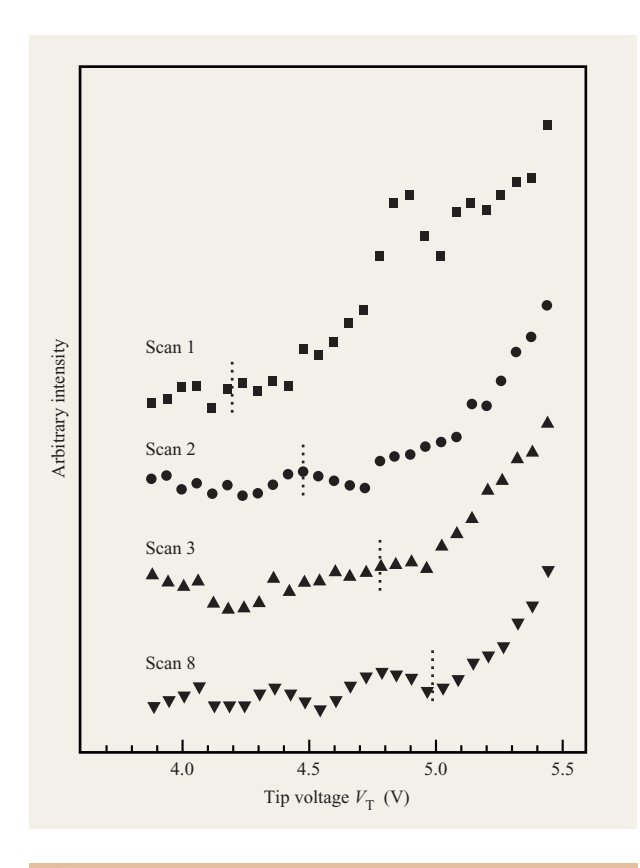


# Figure 5

BEEM spectra for a 7.1-nm-thick oxide taken sequentially on the same spot of the sample. The tip bias  $V_{\rm T}$  was kept below  $-6~{\rm V}$  to suppress the generation of new traps.  $I_{\rm T}=2~{\rm nA}$ . The vertical dotted bars mark the thresholds obtained from computer-aided fits. The spectra were shifted vertically for display purposes. From [28], with permission.

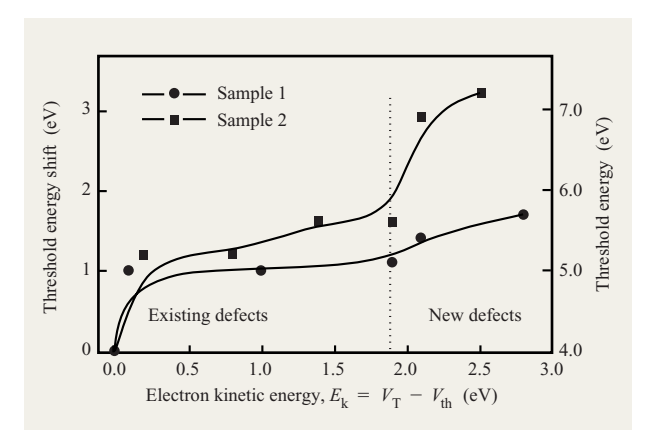


#### Figure 6

Threshold shifts in a 7.1-nm-thick  ${\rm SiO}_2$  layer induced by trapped electrons, as a function of the kinetic energy of hot electrons in the oxide. A second onset of shifts near 2 eV corresponds to generation and filling of new traps. From [28], with permission.

remained below 2 eV ( $|V_{\rm T}|<6$  V). Under these conditions no dependence on the tip bias was noted, which led to the conjecture that the traps were due to defects that existed before the BEEM measurements were performed [28]. The increasing threshold indicated that these pre-existing defects were electron traps. The net shift after saturation was about 1 eV, but could vary from sample to sample, as well as on a local scale of order 5–10 nm [28]. Such variations reflect a distribution in the local charge density of filled traps.

After saturation of the pre-existing traps, hot electrons were injected at energies higher than 2 eV ( $V_T > 6$  V), which resulted in additional shifts in the threshold energies of the BEEM spectra. These shifts were the result of the filling of new traps, which were generated by the hot electrons. The shifts in threshold energy observed as a function of the kinetic energy of the electrons in the conduction band of SiO<sub>2</sub> are shown in Figure 6. The zero threshold shift corresponds to the Pd-SiO, barrier height of 4.08 eV for flatband conditions [29]. The curves in the figure show a soft threshold at  $\sim$ 1.9 eV, beyond which an increase in threshold energies resumes. The increases varied from location to location, an indication of local fluctuations in the density of generated defects. The 1.9-eV threshold value can be directly related to the trap-creation model discussed in the previous section, and involves the breakage of Si-H bonds at the SiO<sub>2</sub>-Si interface [2, 19, 26]. Consequently, one can postulate that the BEEM-generated defects should be located near the Si interface, a premise that is substantiated by the fielddependent experiments discussed next.

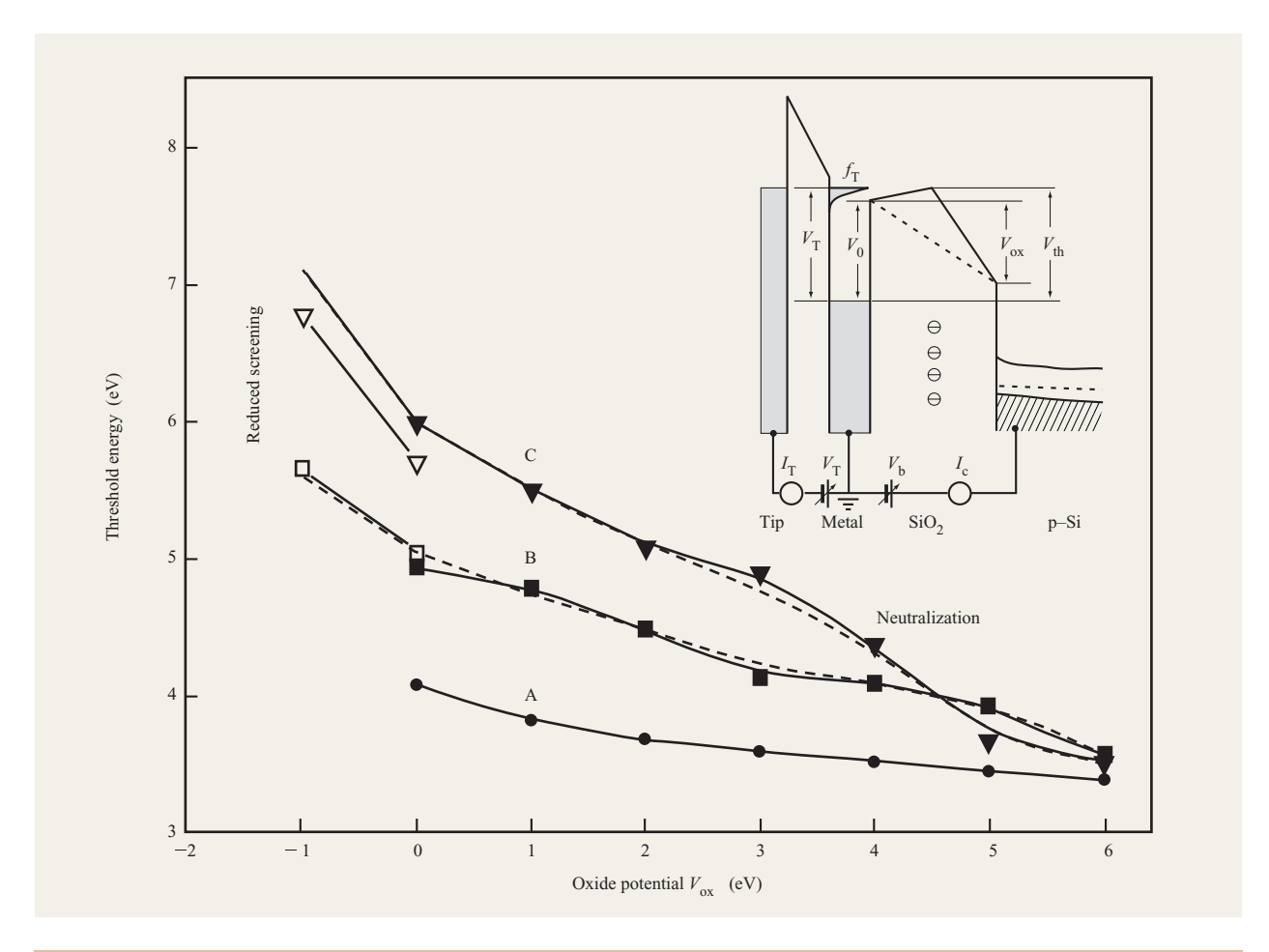


Figure 7

Field-dependent threshold shifts for a 4-nm-thick Pd / 7.1-nm-thick  $SiO_2$  / p-Si(100) sample: Curve A for a charge-free area (only image force lowering); Curve B for charge-saturated pre-existing traps; Curve C for charge-saturated pre-existing traps and stress-induced traps. Threshold error bars are  $\pm 0.05$  eV for B and  $\pm 0.08$  eV for C. Associated energy diagram shown in inset. From [27], with permission.

# Field-dependent threshold shifts

The approximate location of the charge in an SiO<sub>2</sub> gate oxide layer relative to its interfaces can be deduced from the dependence of the thresholds on the applied oxide potential  $V_{\rm b}$ . As can readily be ascertained from the inset of Figure 7, a change of  $\delta V_{ox}$  results in a threshold change of  $\delta V_{\text{th}} = x \delta V_{\text{ox}} / t_{\text{ox}}$ , where  $t_{\text{ox}}$  is the oxide thickness and x the distance of the barrier maximum from the metal-SiO, interface [10]. Thus, the average slope  $\delta V_{\rm th}/\delta V_{\rm ox}$  gives the location of the centroid of the charge distribution. Threshold shifts with applied oxide bias were taken in sets of 36 spectra on previously charge-saturated areas of a 7.1-nm MOS structure [4-nm-thick Pd/7.1-nm-thick SiO<sub>2</sub>/p-Si(100)]. A set of spectra corresponded to a fixed  $V_{\rm h}$  that was incremented in 1-V steps from 0 to 6 V. Each set exhibited a range of threshold values spread over 0.6 eV in a bell-shaped distribution that reflected the local

fluctuations in charge density over the sampled area, at an estimated lateral resolution of 2-3 nm [15]. The distribution shifted rigidly to lower energies with increasing  $V_{\rm h}$  [28], with Curve B in Figure 7 showing the field dependence of the peak of the threshold distribution for the pre-existing traps. The spread in thresholds was reproducible at other charge-saturated areas of the sample, and thus corresponds to a range in charge densities that was characteristic of the oxide layer. The average slope of Curve B is ~0.3 and indicates that the centroid of the charge distribution is 2.1 nm from the metal electrode. However, a closer inspection reveals that the threshold shifts were nonlinear and showed a tendency to saturate prior to a steeper decrease for  $V_{\rm ox} > 5$  V. For  $V_{\rm ox} = 6 \text{ V}, V_{\rm th}$  nearly corresponded to the value of an uncharged sample that was subjected only to image force lowering (Curve A). The concept of image force lowering

524

is discussed further in Section 4. Curve A was obtained from sets of scans on widely separated virgin areas to prevent charge accumulations from affecting the thresholds [29]. The near coincidence of the curves at high oxide biases indicates that the charge-saturated region was temporarily neutralized, since upon returning to  $V_{ox} = 0$ (open symbols),  $V_{th}$  nearly assumed its original value. The neutralization is attributed to anode hole injection, a process that becomes efficient when the electron energy in the SiO, exceeds 5 eV [16], although charge leakage by tunneling, particularly near the anode, may also be a contributory process. For  $V_{\rm ox} < 0$  (open symbols), the threshold increases at a rate greater than the rate one would expect by extrapolating the slope into the negative bias region. As discussed later, the added shift is assigned to a change in electron screening.

The generation and filling of new traps (i.e., kinetic energies >2 V) was observed to be limited as well [28]. This was ascertained by repeatedly scanning a 25-nm × 25-nm area at tip biases as large as -10 V,  $I_{\text{T}} = 2 \text{ nA}$  and  $V_{\rm b} = 0$ , and measuring the thresholds between scans. These stopped shifting after a few scans, which indicated that electron trapping had reached saturation. The oxide field dependence was then measured. Additional electron scattering at the new trap sites resulted in a weak collector current and some scatter in the mean value of the distribution of thresholds. Consequently, only the minimum in the distributions is shown in Figure 7 as Curve C—the maximum lies ~1 eV higher [28]. For the lower bias values, Curve C was shifted nearly 1 eV higher than Curve B, a clear manifestation of additional trapped charge in the oxide. The overall shapes of the two curves are similar. However, the noticeably higher average slope for Curve C ( $\delta V_{\rm th}/\delta V_{\rm ox}\sim 0.6$ ) indicates that the centroid of the charge distribution of the newly generated defects lies closer to the Si interface, specifically 4.2 nm from the metal interface for the 7.1-nm-thick oxide. The decrease in  $V_{th}$  for  $V_{ox} > 3$  V, which ultimately coincides with that of Curve B at 6 V, is due to increasing charge neutralization that is consistent with hole injection processes occurring at the anode. On returning to  $V_b = 0$ , the traps refill within the first spectral scan (open symbols), but do not quite reach the value for the fully saturated traps. Changing  $V_{ox}$  to -1 V had an even more pronounced effect on the threshold shifts than that observed for Curve B. A large fraction of this shift can be ascribed to changes in screening at the oxide-semiconductor (O-S) interface.

# In-depth distributions of oxide charge

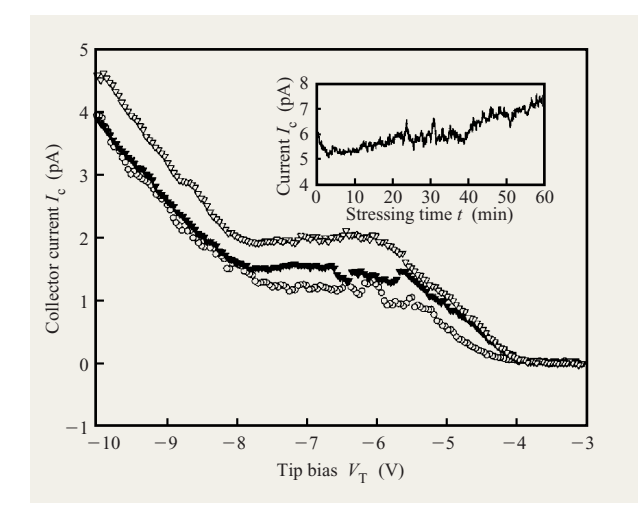
The charge distribution can be modeled uniquely by calculating the field dependence of the thresholds with a trial distribution and subsequently adjusting it until the details of the nonlinear threshold shifts of Figure 7 are duplicated [28]. A single  $\delta$ - or sheet charge exhibits a

strictly linear field dependence of the threshold energy at low to moderate fields. Changes in slope, on the other hand, indicate that the oxide charge is distributed. Details of the procedure have been presented elsewhere, and only an outline is given here [27, 28]. The trapped charge in the oxide is modeled by a series of equally spaced sheet charges. The potential  $\Phi_i(x)$  is calculated for each sheet charge subject to boundary conditions that the potential vanishes at both interfaces. For the O-S interface this condition reflects that the p-Si is in accumulation for positive  $V_{\rm h}$  (injected electrons are accelerated toward the Si substrate). The boundary conditions are satisfied by the method of images, provided that multi-image charges, i.e., image charges of image charges, are included. These arise due to the presence of the second interface. The potentials  $\Phi_n$  due to the *n* individual sheet charges are summed, viz.,  $\Phi_a(x) = \Phi_1(x) + \Phi_2(x) + \cdots + \Phi_n(x)$ , and then added to the field-dependent oxide potential to give the net potential U(x):

$$U(x) = eV_0 - \frac{eV_{ox}x}{t_{ox}} - \frac{e}{16\pi\varepsilon x} - \frac{e\rho}{16\pi\varepsilon (t_{ox} - x)} + \Phi_q(x).$$
 (1)

Here  $eV_0$  is the charge-free oxide barrier height,  $eV_{\rm ox}x/t$  the field-effect contribution, and  $e/16\pi\epsilon x$  and  $e\rho/16\pi\epsilon (t-x)$  represent, respectively, the dynamic image force lowering at the metal-oxide (M-O) and O-S interfaces. Furthermore,  $\rho=(\varepsilon_{\rm s}-\varepsilon_{\rm ox})/(\varepsilon_{\rm s}+\varepsilon_{\rm ox})$ , where  $\varepsilon_{\rm s}$  is the effective dielectric constant at the Si interface, and  $\rho$  reflects the screening effectiveness of the Si. In the absence of free carriers,  $\rho=0.70$ . However, during accumulation, with free carriers at the interface,  $\varepsilon_{\rm s}>11.9$ , its bulk value, with  $\rho$  approaching unity the more the interface region approaches metallic characteristics.

The potential  $U(x/t_{ox})$  of Figure 4(b) is due to a distribution of negative charge represented by seven sheet charges shown in the middle of the figure. It is readily seen that with increasing positive bias, the peak position in  $U(x/t_{ox})$  moves closer to the M-O (left) interface, a nonlinear change associated with a distributed charge density. The distribution shown is that of the generated defects used to calculate the field dependence in the fits to the experimental data shown in Curve C of Figure 7. The actual fit, shown by the dashed line, also required the inclusion of negative charge residing in the pre-existing traps [27]. These were modeled first, with a charge distribution peaked at the M-O interface, resulting in the fit shown by the dashed line of Curve B. The additional decrease observed in the experimental data at higher oxide bias in both Curves B and C could be simulated only by assuming charge neutralization, which was modeled by reducing the occupancy in the sheet charges to zero for the generated defects, while maintaining a reduced charge density in the pre-existing traps [27]. Neutralization, most



BEEM spectra of a 5-nm-thick Pd / 2.8-nm-thick  $SiO_2$  / n-Si(100) MOS structure: prior to electrical stressing (open circles), after injection of 19 nC (open triangles), and following injection of 41 nC (solid triangles). The stressing was carried out at  $V_T = -13$  V and  $V_b = 0$ . The tip bias imparts the electrons in the oxide with a kinetic energy of 9 eV. The inset shows a representative spectrum of stressing current vs. time at the same levels of  $V_T$  and  $V_b$  after injecting a charge of 21.6 nC. Adapted from [31], with permission.

likely by anode hole injection, did not eliminate the traps, which were refilled upon returning to zero bias conditions, while maintaining the tip bias  $V_{\rm T}$  below 6 eV to eliminate the possibility of generating new defects. The resulting thresholds are shown by the open symbols at  $V_{\rm ox}=0$ . Subsequently changing  $V_{\rm ox}$  to -1 V produced the large threshold shifts depicted in Figure 7. Under these bias conditions, the p-type Si becomes depleted at the interface, which reduces its screening ability. This reduction can be modeled by reducing the screening factor  $\rho$  from 1 (metallic) to 0.75, as shown by the dotted lines for  $V_{\rm ox}<0$ . This value is in good agreement with  $\rho=0.70$  obtained using an optical dielectric constant of 2.1 for the SiO, layer.

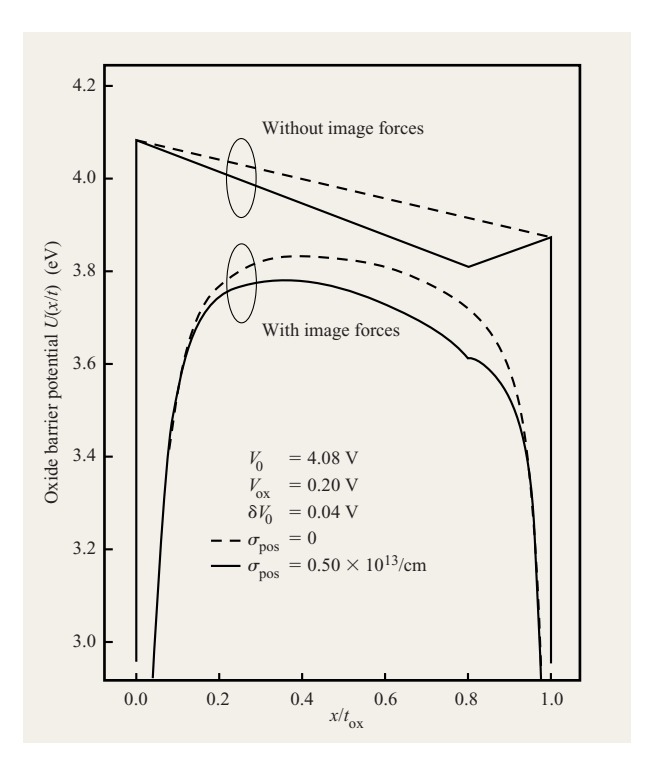
The modeling of the field dependence of the threshold leads to the following conclusions: 1) The pre-existing defects are close to the M–O interface and exhibit a decreasing density away from the interface. From the spread in threshold fluctuations, the net charge density is in the range of  $(0.77-2.8)\times 10^{13}~{\rm cm}^{-2}$ . 2) The generated traps are located closer to the O–S interface, with a total density spread of  $(1.9-3.6)\times 10^{13}~{\rm cm}^{-2}$ . 3) The large threshold increases for negative values of  $V_{\rm ox}$  can be modeled in terms of a decrease in free-carrier screening at the O–S interface. 4) The threshold reductions under high

bias are consistent with charge neutralization by anode hole injection.

#### • Positive charge in ultrathin oxides

In contrast to the thicker oxides just discussed, electrical stressed oxides having thicknesses less than about 4 nm do not exhibit a change in threshold that can be attributed to buildup of negative charge in the oxide. The lack of a measurable threshold shift, shown in Figure 8, suggests that any charge, if present, is positive and furthermore is located near the O-S interface, where its influence on the barrier height is largely suppressed by image force effects, as can be judged upon inspecting Figure 9. The presence of positive charge near the Si interface was also concluded from F-N stressing experiments [30]. In BEEM experiments, an increase in the collector current is observed after moderately stressing the oxide. This is shown in Figure 8, where the open-circle curve represents the initial scan on a previously unexposed surface of the sample, and the open-triangle curve represents the scan after the oxide was stressed at the same spot by raising the tip bias to -13 V. The collector current increased, as shown in the inset of Figure 8, from ~5 pA at the start of the stressing to 7.5 pA after the 60-minute stress interval [31]. No shifts in thresholds were observed within a measurement uncertainty of  $\pm 0.05$  V. The absence of threshold shifts together with the increase in the collector current suggests the presence of positive charge, which provides an accelerating potential that increases the transmission probability [9]. The expected effect of a positive charge in the oxide on the potential profile can be seen in Figure 9. Although a small decrease in the barrier height is indicated, the main consequence of the positive charge is an increase in the average oxide potential (slope), enhancing the transmission probability [9]. A second stress cycle under the same conditions raised the total injected charge to 41 nC. The BEEM spectrum taken immediately afterward (Figure 8, solid-triangle curve) resulted in an overall decrease in intensity. Since an increase in the threshold was not observed, the decrease in intensity is not due to a buildup of negative charge, as discussed for the thicker oxides, but rather to the creation of additional scattering centers that reduce the transmission probability, an effect also observed for thicker oxides [31].

The enhancement in the transmission can also be seen in the BEEM image, which was simultaneously recorded with the topographic or STM image; both are shown in **Figure 10**. The STM image shows no evidence of surface damage in the morphology of the deposited Pd layer, whose nodular structure was not affected by the stressing. Contrast for the BEEM image was provided by the local variations in the collector current  $I_c$  and thus represents an image of the electron transmission characteristics.



#### Fiaure 9

Calculated effect of a positive sheet charge  $\sigma_{\rm pos}=5\times10^{12}/{\rm cm^2}$  placed at  $0.2t_{\rm ox}$  from the O–S interface (0.56 nm for the 2.8-nm-thick oxide); x is the distance from the M–O interface. When image forces are included (the lower two curves), the calculation indicates that the kinetic energies of the electrons near the O–S interface should be substantially greater. The further decrease with the addition of positive charge increases the transmission probability, accounting for the increase in collector current for moderate stressing indicated in the inset of Figure 8.

Additional image contrast arises from the surface morphology of the metal film, an unavoidable problem associated with the STM injection geometry. The brighter area near the center of the BEEM image is due to the enhancement in transmission resulting from the generation of positive charge. The area of enhanced transmission is  $\sim 1.3 \times 10^{-11}$  cm<sup>2</sup>, which is larger than the area exposed to direct injection by the STM tip. The increase is a consequence of multiple scattering of the electrons in both metal and oxide layers, as well as tip drift during the long stressing times. The total injected charge density was  $3 \times 10^3$  C for  $10 < |V_{\rm T}| < 13$  V, and  $V_{\rm b} = 0$ . The kinetic energy of the electrons in the oxide for this range of  $V_{\scriptscriptstyle \rm T}$ corresponds to 6-9 eV. As an aside, energies of this magnitude are achievable with F-N injection only by pulsing, since the fields required to reach such energies solely by field acceleration are ~50 MV/cm for a 2.8-nmthick oxide. However, such energetic electrons are not

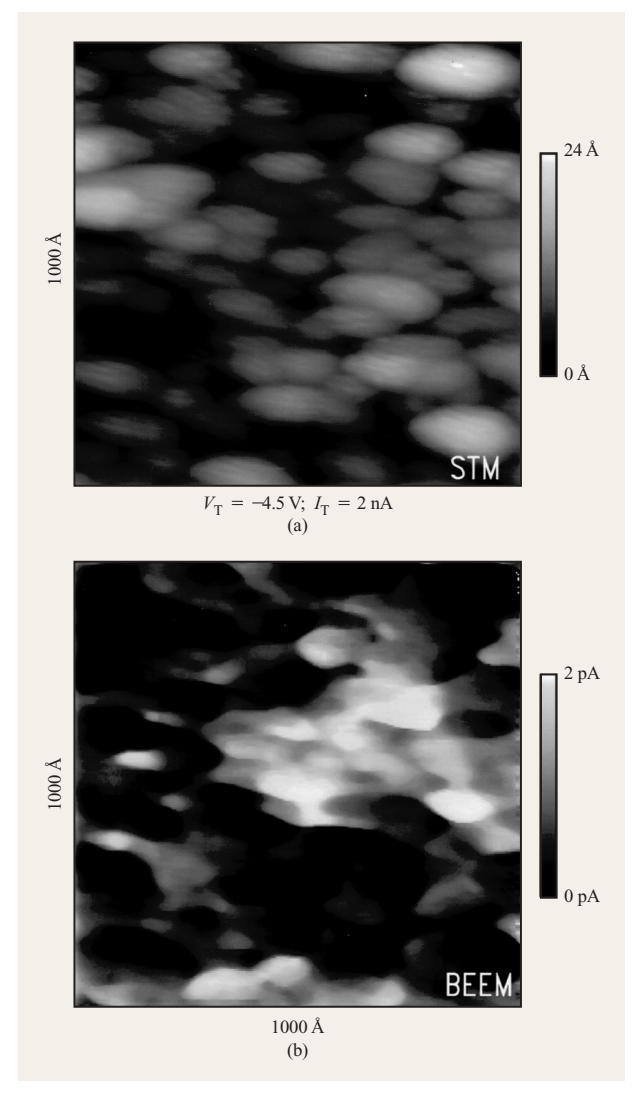
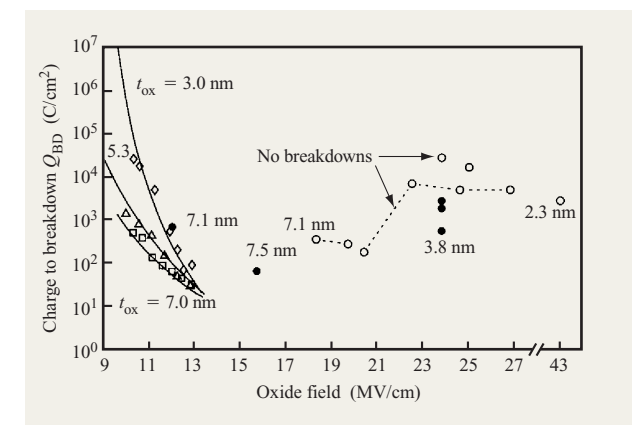


#### Figure 10

STM topographic image (a) and BEEM image (b) of a 5-nm-thick Pd / 2.8-nm-thick SiO $_2$  / n-Si(100) structure after stressing under the conditions of Figure 8. Adjacent gray scales indicate the contrast ranges. The images were obtained with  $V_{\rm T}=-4.5$  V,  $I_{\rm T}=2$  nA, and  $V_{\rm b}=0$ . The stressed area is seen as a higher-transmission region because of the presence of stress-induced positive charge. From [31], with permission.

needed to generate positive charge, which is already evident from the observed increase in  $I_c$  following the injection of 0.01 nC at a kinetic energy of 1 eV  $(V_T = 5 \text{ V})$  [31].

The localized suppression of the transmission in BEEM images following the stressing of thick oxides has been reported by Kaczer et al. [10] and subsequently by Wen et al. [31]. The observed decrease in transmission was



Normalized charge to breakdown at room temperature as a function of average electric field for indicated oxide thicknesses. The data corresponding to the open symbols on the left were obtained through field stressing (injection by Fowler–Nordheim tunneling from a polysilicon gate); the solid lines are model calculations adapted from [33], with permission. The solid circles represent data on occasional oxide failures achieved with BEEM for 3.8-nm-thick and 7.1- to 7.5-nm-thick oxide layers; the open circles represent stress levels achieved without breakdown. The energies of the STM-injected electrons were converted to the equivalent field necessary to achieve those values by field acceleration. Adapted from [15], with permission.

attributed to the buildup of negative charge, as discussed above in the section on electron traps. The same mechanism of electron trap formation is believed to occur as well in the thinner oxides. However, electrons captured in the traps are believed to leak out by tunneling to conduction band states in the adjacent Si, a process achieved in the thicker oxides only by applying large electric fields. For the thin oxides, the absence of the negative charge reveals the existence of the positive charge, whose levels must lie near or above the Fermi level of the Si.

# • Oxide degradation and breakdown

From the trap-generation experiments discussed above, one could surmise that areas of high densities of negative trapped charge observed in the thicker oxides ( $\sim 5 \times 10^{13} / \mathrm{cm}^2$ ) should be conducive to local breakdown upon further stressing. However, many attempts at inducing local breakdown through additional injection of hot electrons have demonstrated that destructive breakdown is seldom achieved. In the few instances when breakdown occurred, as manifested by a drastic reduction in the local oxide potential, the net injected charge, referred to as charge to breakdown, or  $Q_{\rm BD}$ , was orders of magnitude larger than those reported for F–N stressing of MOS

capacitors [15]. We present here only the salient results of these studies; for details the reader is referred to Reference [15].

Breakdown studies were performed on oxides having thicknesses in the range of 2.3-7.1 nm, with some of the most detailed studies on 3.8-nm-thick and 7.1-nm-thick oxides. In these experiments, the tip of the STM was positioned either on a previously unexposed area of the sample, or on areas for which the trap states had been saturated, as discussed above in the section on electron traps. The tip bias and current were then set to predetermined values (7 <  $V_{\rm T}$  < 13, 2 <  $I_{\rm T}$  < 5 nA), and the collector current was integrated to determine the total charge injected into the oxide. The stressing process was repeatedly interrupted to measure the threshold position by taking a BEEM spectrum. The thresholds for the 3.8and 7.1-nm-thick oxides increased initially but reached a plateau, which is indicative of the trap-generation and filling process discussed above. If the stressing proceeds toward an eventual breakdown, as was observed for a 3.8-nm-thick oxide [15], the thresholds begin to decrease again, and an increase in the overall collector current is observed. This second stage of stressing has been referred to as the pre-breakdown stage. The decrease in thresholds is the result of the neutralization of the trapped negative charge through either leakage or positive charge generation. This neutralization is the result of a local "thinning" of the oxide, that is, the formation of a conductive path due to the presence of overlapping states that start at the O-S interface [2, 32]. Additional stressing quickly leads to a total collapse of the oxide barrier, an event characterized by a threshold of only 1 eV. The latter event has been termed the breakdown stage, with the net collector current integrated to a point just prior to the collapse defined as  $Q_{\rm BD}.$  The injected charge density can be obtained from the spread in the injected beam at the SiO<sub>2</sub>-Si interface, as calculated by Monte Carlo methods and illustrated in Figure 3.

A common method of representing stress-to-failure results obtained by F-N injection is to plot  $Q_{\mathrm{BD}}$  vs. oxide field, as shown by the open symbols and lines in Figure 11 [33]. In order to compare BEEM stressing results to these data, the energies of electrons during BEEM stressing were converted to electric fields that would be required to achieve the same energies at the anode with F-N injection. This conversion assumes that the breakdown process depends predominantly on the energy of the electrons, and not on the field. With this premise, the BEEM data actually represent an underestimate of the stressing conditions relative to F-N, since for the latter the equivalent energy is reached only at the anode, whereas in BEEM the energy of an electron is more uniform throughout its traversal of the oxide. The results of the few breakdowns observed are shown by the solid

528

circles in Figure 11. The much more numerous stress experiments that did not lead to breakdowns are shown by open circles. The abscissa values (not true  $Q_{\rm BD}$  values) of the latter were limited by inevitable tip drifts away from the injection point. It appears from examination of Figure 11 that BEEM-initiated local breakdowns, when they occur, lie appreciably above an extrapolated curve of data obtained in a conventional, large-area stressing experiment. The latter results were deemed to be limited by "intrinsic" properties of the oxide [34]. Our results clearly contradict this view, indicating instead that an intrinsic limit has not yet been reached, and that even in our case breakdowns are still limited by randomly distributed defects/impurities of still unknown origin.

# 4. BEEM studies of fundamental oxide parameters

A couple of salient examples of the unique capabilities of BEEM in the study of fundamental physical phenomena are discussed in this section. They are the dynamic response of an  $\mathrm{SiO}_2$  gate oxide layer to a moving electron, and the determination of the layer's conduction-band effective mass and its dispersion with energy.

• Dynamic response to a moving charge: Effective dielectric constant

An electron injected from a gate conductor into a gate oxide experiences the effects of the free electrons in the conductor, which move away from the interface in response to the presence of the electron in the oxide, leaving a net positive charge near the interface. This action, termed screening, results in an attractive potential sensed by the electrons in the oxide. The screening is often and quite adequately described by the classical method of images [35], an approach that is valid to distances of separation between metal and charge of the order of a Bohr radius ( $\sim 0.05$  nm), below which a quantum-mechanical description becomes necessary [36]. The changes in the potential sensed by an electron from such image force effects are further modified by the net oxide potential  $V_{\rm ox}$ , in what is referred to as the Schottky effect [37]:

$$\Phi_{\rm im}(x) = eV_0 - eV_{\rm ox}\frac{x}{t_{\rm ox}} - \frac{e^2}{16\pi\varepsilon_0\varepsilon_{\rm ox}x},\tag{2}$$

where  $t_{\rm ox}$  is the thickness of the oxide layer,  $\varepsilon_0$  the permittivity of free space, and  $\varepsilon_{\rm ox}$  the effective dielectric constant of the oxide. The potential is shown by the dashed curve in Figure 1(b) and by the lower dashed curve in Figure 9. The latter includes the image force corrections due to both interfaces. The lowering  $\delta V_0$  of the threshold  $V_0$  and the location of the maximum  $x_m$  in

 $\Phi_{\text{im}}$  is readily obtained by minimizing the differential of Equation (2). One thus obtains

$$\delta e V_0 = \left[ \frac{e V_{\text{ox}}}{4\pi \varepsilon_0 \varepsilon_{\text{ox}} t_{\text{ox}}} \right]^{1/2}; \tag{3a}$$

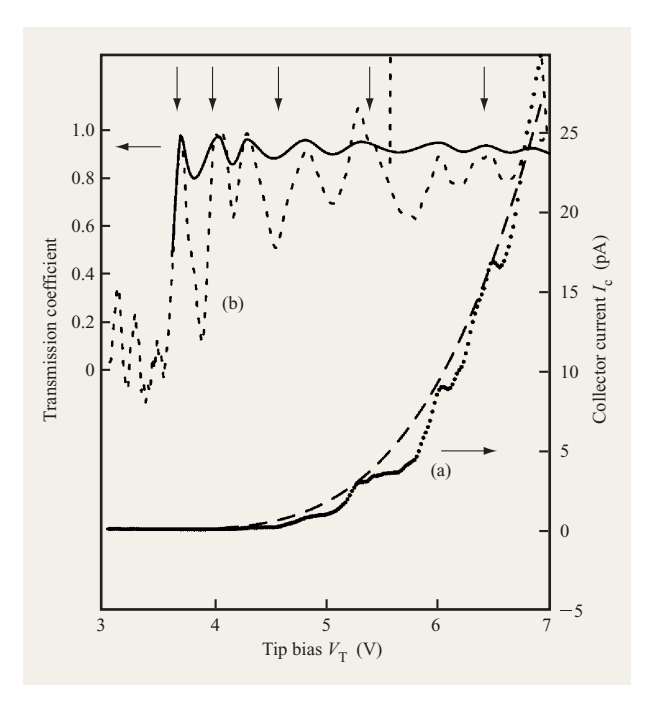
$$x_{m} = \left[\frac{et_{\text{ox}}}{16\pi\varepsilon_{0}\varepsilon_{\text{ox}}V_{\text{ox}}}\right]^{1/2}.$$
 (3b)

In the absence of an oxide charge, the effective barrier height at the metal-oxide interface is given by  $eV_{\text{th}} = eV_0 - e\delta V_0$ , with  $V_0$  representing the interface barrier height under flatband conditions ( $V_{ox} = 0$ ). The root dependence of  $eV_{th}$  on  $V_{ox}$  is implied in Figure 7(a) for the threshold shifts at a charge-free location on the sample [27]. A linear dependence on  $V_{\rm ox}^{1/2}$  is premised on the condition that the effective dielectric constant  $\varepsilon_{ox}$  is fieldindependent over the range of applied  $V_{ox}$  values. Such a relationship has indeed been observed [29, 38], and the value of  $\varepsilon_{ox} = 2.74$  was obtained from it. This value lies between the static value of 3.9 and the optical or highfrequency value 2.15. The latter value was obtained from internal photoemission experiments on MOS structures [39]. This technique responds to contributions from more energetic electrons, which, in contrast to the low-energy electrons at the threshold in BEEM measurements, do not excite the lattice modes of SiO, that enhance its dielectric constant at low excitation energies. Support for the validity of the BEEM-determined dielectric response has been obtained from a theoretical treatment of a classical particle subject to a time-dependent potential in a polarizable medium. In the model the optical phonon modes of SiO, were assigned to the dielectric [29, 38], which yielded a value for the dielectric response  $\varepsilon_{ox}$  = 2.69, in close agreement with experimental results. The results indicated that even moderately energetic electrons sense the presence of the optical phonon modes.

The linear relationship of  $V_{\rm th}$  on  $V_{\rm ox}^{1/2}$  attests to the validity of image force effects in MOS transport. This issue was realized early in investigations of F–N tunneling experiments, but is now generally ignored in nearly all transport studies on MOS structures. The consequences of this omission are addressed in the next section.

 $\bullet$  The effective conduction-band mass of an SiO  $_2$  gate oxide layer and its dispersion

The effective mass  $m_{\rm ox}$  of conduction-band electrons in an SiO<sub>2</sub> gate oxide layer is a parameter that enters into the description of virtually every aspect of hot-electron transport in MOS-based structures and devices [40]. The mass directly affects the electron-phonon coupling strengths that determine scattering rates in the layer, which in turn determine the thermalization of hot electrons [14], charge trapping/detrapping phenomena



(a) BEEM spectrum for a 1.8-nm-thick W / 3.0-nm-thick SiO $_2$  / p-Si(100) MOS structure (dotted curve) with estimated unmodulated collector current component  $I_c^0$  shown by a dashed line. (b) "Experimental" transmission coefficient,  $I_c/I_c^0$  (dotted curve), compared to  $\tau(E)$  calculated with a dispersive mass (solid curve). Vertical arrows mark interference maxima for  $\tau(E)$  calculated assuming a fixed mass  $m_{\rm ox}=0.42~m_0$ . From [54], with permission.

[2], and ultimately device degradation processes [3]. Nevertheless,  $m_{ox}$  has not been measured unequivocally, and considerable disparities have been reported [41-43]. Complicating this issue is a prevailing tendency to interchange  $m_{ox}$  with masses derived from tunneling experiments, an unfortunate misuse that need not be elaborated further. More significantly, as most hotelectron phenomena in MOS structures are studied under high-field conditions, with F-N tunneling being the dominant injection technique used, the electrons are subject to dynamic events over a position-dependent range of kinetic energies. Hence, knowledge of the energy dependence of the electron interactions is needed to simulate electron transport. Yet a direct measurement of the energy dependence of transport parameters from F-N experiments is virtually impossible, since only energyaveraged values have been extracted. The suggestion that  $m_{ox}$  is dispersive, i.e.,  $m_{ox} = m_{ox}(E)$ , where E is the kinetic energy of the conduction-band electron, has been made by Maserjian [41] and subsequently addressed by others [40, 44].

A dispersive  $m_{ox}$  is also evident from band-structure calculations for all polytypes of quartz [45]. However, a direct measurement, based on BEEM over a kinetic energy range of 3 eV, has been reported only recently [46]. The method for obtaining  $m_{ox}(E)$  is based on the observation of quantum interference (QI) oscillation in the BEEM current and its theoretical modeling with  $m_{ox}(E)$  adjusted to fit experimental data. The QI oscillations in the BEEM current  $I_c$  arise from interference effects of the electron wave function in the oxide conduction band [43, 44], akin to those observed in F-N experiments [41, 42, 47–51]. In the simplest model of a rectangular potential barrier of height U, maxima in the quantum-mechanical transmission coefficient  $\tau(E)$  are found at  $(E-U)^{1/2} = n\pi\hbar/d(2m)^{1/2}, n = 1, 2, 3\cdots$  [52].

A BEEM spectrum for a MOS structure consisting of 1.8-nm-thick W/3-nm-thick SiO<sub>2</sub>/p-Si(100) is shown as the dotted curve region (a) of Figure 12. An oscillatory structure is clearly observable. The STM tip bias at threshold was -3.77 V. A bias  $V_b = 0.3$  V (substrate positive) was applied across the oxide to ensure flatband conditions [53]. All of the spectra shown in the figure were obtained from areas of the sample not previously subjected to electron injection. As discussed above, prior exposures, particularly for  $V_{\scriptscriptstyle \rm T} > 6$  V, can generate positive oxide charge whose random distribution alters and even suppresses the OI structure. The energetic positions of the interference maxima, although measurable from the raw data, were more accurately determined by assuming that I could be represented as a product of the transmission coefficient  $\tau(E)$  and an unmodulated component of the collector current  $I_c^0$ :  $I_c(E) = \tau(E)I_c^0(E)$ . The collector current could be approximated by a simple power-law curve tangential to the maxima in the BEEM spectrum, as shown by the dashed curve in region (a) of Figure 12. By dividing  $I_c$  by  $I_c^0$ ,  $\tau(E)$  could then be obtained, with the results shown by the dotted curve in region (b). This curve represents approximately the "experimental"  $\tau(E)$ , from which the interference maxima could be obtained.

We next summarize the calculation of  $\tau(E)$  and the procedure to match the maxima with those of the "experimental"  $\tau(E)$ . Details of the numerical solution of the one-dimensional Schrödinger equation with the appropriate potential barrier and boundary conditions are discussed elsewhere [46]. The barrier was modeled by a multistep potential approximation that included image force corrections arising from both the metal–SiO<sub>2</sub> and SiO<sub>2</sub>–Si interfaces. Effective masses of  $m_0$  and  $0.19m_0$  were assumed for the conduction-band electrons of the metal and the Si, respectively. The results of calculating  $\tau(E)$  with a constant mass [43], represented in region (b)

 $<sup>^{1}\</sup>tau(E)$  represents the transmission coefficient in the ballistic limit that ignores electron–phonon interactions, an approximation suitable for the thin SiO $_{2}$  films used for the QI studies.

of Figure 12 solely by arrows marking the maxima, shows agreement with experiment only for the first two maxima, to which the solution was intentionally fitted by setting  $m_{\rm ox} = 0.42 m_{\rm o}$ . Consequently, the mass was adjusted so that each maximum agreed with the experimental one, thereby yielding a discrete set of dispersing masses  $m_{ox}(E_i)$  at peak energies  $E_i$ . The resulting  $\tau(E)$  is shown by the solid curve in region (b) of Figure 12. The values of  $m_{ox}(E_i)$  were then used to obtain the dispersion, which is shown by the central curve in Figure 13. Here we have subtracted the threshold energies to show the dispersions as a function of the kinetic energy (KE) of the conduction-band electrons in SiO<sub>2</sub>. Figure 13 also depicts the mass dispersion obtained from Monte Carlo (MC) simulations of the attenuation lengths in SiO, (open symbols) [54]. Although the agreement with the BEEM results is marginal and attributable to arbitrarily setting  $m_{ox} = 0.5m_0$  at KE = 1.5 eV in the MC calculations, it is reassuring that the changes in mass over comparable energy intervals are quite close.

We have also determined the dispersion for a 2.3-nmthick SiO, layer which was thermally grown on p-Si(100) and covered with a 4-nm-thick Pd layer [46]. The dispersion observed for this sample is shown by the uppermost curve in Figure 13. Its upward displacement relative to the 3.0-nm-thick oxide cannot be accounted for by uncertainties in the parameters, particularly in their thicknesses. Consequently, we attribute the difference in the dispersions to thickness-related phenomena, such as an onset of band-structure changes. The overall increase in  $m_{ox}(E)$  for the thinner oxide is consistent with a narrowing of the bands due to the decreasing dimensionality [55]. The range of the dispersions in all three cases, which are comparable in magnitude, implies considerable nonparabolicity in the conduction bands of SiO<sub>2</sub>. The reduced dispersion at low KE, particularly for the 3.0-nm-thick oxide, indicates an initial constancy of  $m_{ox}(E)$  that implies a parabolic band behavior near the bottom of the conduction band. The value here of  $0.44m_0$  is close to the best estimates for the tunnel mass  $m_{\star} = 0.42 m_{0}$ near the top of the gap [41, 56], and is consistent with the smooth transition between a Franz-type band dispersion in the gap and the bottom of the conduction band [41]. By integrating the mass dispersions, one readily obtains the band dispersions, as shown in Figure 14. To aid the eye, a parabolic dispersion (dashed curve) has been superimposed to emphasize the deviations from parabolicity. The estimated conduction band obtained by pseudopotential theory for  $\alpha$ -quartz is shown as a dotted line [57]. The corresponding mass of  $0.3m_0$  appears to be inconsistent with experimental results for amorphous SiO<sub>2</sub>.

Indicated on the right ordinate of Figure 13 near  $m_{\rm ox} = 0.85 m_0$  are values obtained previously from QI in FN-injection experiments [41, 42]. Their magnitude

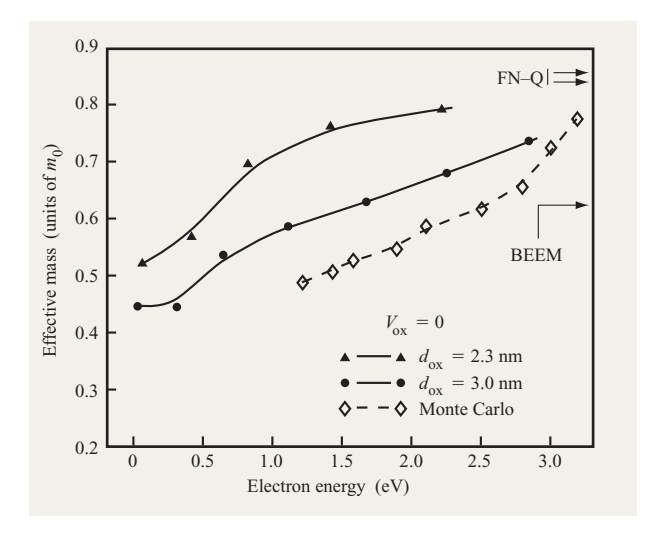


# Figure 13

Effective mass vs. electron energy, determined from quantum interference oscillations in BEEM spectra (solid curves). Also shown is the dispersion derived from Monte Carlo simulations of experimentally determined electron mean free paths (dashed curve). Adapted from [54], with permission.

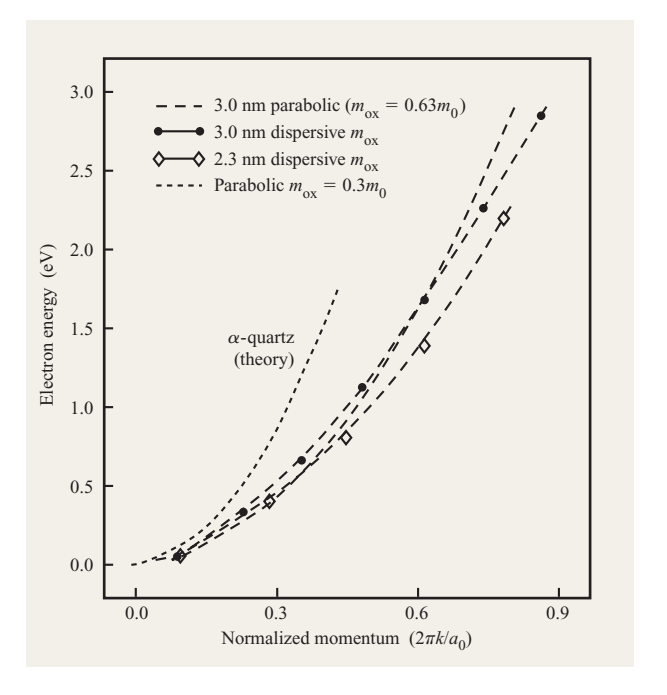


# Figure 14

Electron energy vs. normalized momentum, obtained from integrating the data of Figure 13. The dotted curve is a theoretical calculation for  $\alpha$ -quartz, from [57], reproduced with permission. To calculate the dispersions, use was made of an effective lattice constant  $a_0 = 0.716$  nm, equal to that of cubic  $\beta$ -crystobalite.

is considerably larger than the  $0.63m_0$  value obtained recently by BEEM for a 2.8-nm-thick oxide [43], which was deduced from a single mass fit to data inferior to the results reported here. Nevertheless, its value agrees well with the energy-averaged dispersive mass for the 3.0-nm-thick layer. The origin of the discrepancies with the F-N results can readily be attributed to their greater sensitivity of  $m_{ox}$  to uncertainties in the F-N parameters, in particular the barrier height and its modification by image force corrections, which were neglected [54].

# 5. Concluding remarks

In this review we have attempted to show the power and versatility of BEEM in addressing critical issues of oxide physics and oxide reliability on a microscopic scale. The technique, in conjunction with modeling, has provided new insights into electron transport in ultrathin SiO, layers, including the importance of screening (image force effects) both in electron-phonon interactions for thin oxides and in the determination of the effective electron mass. The role of low-frequency vibrational interactions on the dynamic response to a moving charge, as expressed by an effective dielectric constant, has been elucidated experimentally and confirmed by modeling. The energetics of defect generation and its effect on electron transport have been investigated, with electron trapping dominating in the thicker films and positive charge generation controlling transport in ultrathin SiO<sub>2</sub> layers. One essential observation is that the oxides are extremely difficult to break down by local electric stressing, and that the breakdown process continues to be dominated by extrinsic factors. In the area of fundamental physical properties, the observation of QI oscillations in the BEEM current permits an absolute determination of the dispersion of the conduction-band mass of SiO<sub>2</sub>. The mere existence of dispersion attests to a description of an atomic short-range correlation that supports the concept of a band structure [40]. One of the major conclusions that underlie this work is further substantiation that the amorphous SiO, layers exhibit many if not most of the characteristics of crystalline solids, including well-defined vibrational (optical) properties, and band structural properties, as well as the concept of an effective mass and its dispersion with energy.

# **Acknowledgments**

The work described here could not have progressed to the level described were it not for the contributions of many colleagues. My appreciation is particularly directed (in alphabetical order) to Andreas Bauer of the Free University of Berlin, who as a predoctoral student first carried out BEEM on SiO<sub>2</sub>-MOS structures; to Doug Buchanan, Ed Cartier, Chris D'Emic, and Dennis Newns of this laboratory, Doug for his many suggestions and

contributions to sample preparation and characterization, Ed for the extensive Monte Carlo simulations, Chris for the growth of the oxides, and Dennis for his physical insights and help in formulating the dynamic response of electrons in dielectrics; to Michael Prikas, whose diligence kept the lab running smoothly; to Andreas Schenk of the Swiss Federal Institute of Technology in Zürich, whose modeling of conduction-band transport led to quantifying the effective conduction-band mass in SiO<sub>2</sub>; and to H. J. Wen, a former postdoctoral fellow who performed many of the BEEM measurements discussed here and contributed decisively to their interpretations.

\*\*Trademark or registered trademark of Burleigh Instruments, Inc.

#### References

- National Technology Roadmap for Semiconductors, Semiconductor Industry Association, 1997 edition.
- D. J. DiMaria, E. Cartier, and D. Arnold, *J. Appl. Phys.* 73, 3367 (1993); D. Arnold, E. Cartier, and D. J. DiMaria,
   *Phys. Rev. B* 49, 10278 (1994).
- E. Cartier, Microelectron. Reliab. 38, 201 (1998); E. Cartier and D. J. DiMaria, Microelectron. Eng. 22, 207 (1993).
- 4. Y. Taur, C. H. Wann, and D. J. Frank, Proceedings of the IEEE International Electron Devices Meeting, 1998, p. 789.
- W. J. Kaiser and L. D. Bell, *Phys. Rev. Lett.* 60, 1406 (1988).
- M. Prietsch, *Phys. Rep.* 253, 163 (1995); L. D. Bell and V. Narayanamurti, *Curr. Opin. Solid State Mater. Sci.* 3, 39 (1998).
- D. K. Guthrie, P. N. First, T. K. Gaylord, E. N. Glytsis, and R. E. Leibenguth, *Appl. Phys. Lett.* 71, 2292 (1997) and 72, 374 (1998).
- 8. M. T. Cuberes, A. Bauer, H. J. Wen, M. Prietsch, and G. Kaindl, *Appl. Phys. Lett.* **64**, 2300 (1994).
- R. Ludeke, A. Bauer, and E. Cartier, J. Vac. Sci. Technol. B 13, 1830 (1995); Appl. Phys. Lett. 66, 730 (1995).
- B. Kaczer, Z. Meng, and J. P. Pelz, *Phys. Rev. Lett.* 77, 91 (1996);
   B. Kaczer and P. J. Pelz, *J. Vac. Sci. Technol. B* 14, 2864 (1996).
- 11. K. F. Schuegraf and C. Hu, J. Appl. Phys. 76, 3695 (1994).
- M. Depas, B. Vermeire, P. W. Mertens, M. Meuris, and M. M. Heyns, Semicond. Sci. Technol. 10, 753 (1995).
- R. Ludeke and A. Bauer, J. Vac. Sci. Technol. A 12, 1910 (1994).
- M. V. Fischetti, D. J. DiMaria, S. D. Brorson, T. N. Theis, and J. R. Kirtley, *Phys. Rev. B* 31, 8124 (1985).
- R. Ludeke, H. J. Wen, and E. Cartier, J. Vac. Sci. Technol. B 14, 2855 (1996).
- D. J. DiMaria, E. Cartier, and D. A. Buchanan, J. Appl. Phys. 80, 304 (1996), and references therein.
- 17. P. Solomon, J. Vac. Sci. Technol. 14, 1122 (1977).
- D. J. DiMaria, T. N. Theis, J. R. Kirtley, F. L. Pesavento,
   D. W. Dong, and S. D. Brorson, *J. Appl. Phys.* 57, 1214 (1985).
- 19. E. Harari, Appl. Phys. Lett. 30, 601 (1977).
- 20. P. Olive, T. N. Nguyen, and B. Riccó, *IEEE Trans. Electron Devices* 38, 527 (1991).
- P. P. Apte, T. Kubota, and K. C. Saraswat, J. Electrochem. Soc. 140, 770 (1993).
- L. K. Han, M. Bhat, D. Wristers, J. Fulford, and D. L. Kwong, Proceedings of the IEEE International Electron Devices Meeting, 1994, p. 617.

- S.-H. Lee, B.-J. Cho, J.-C. Kim, and S.-H. Choi, Proceedings of the IEEE International Electron Devices Meeting, 1994, p. 605.
- C. H. Lin, J. Cable, and J. C. S. Woo, *IEEE Trans. Electron Devices* 42, 1329 (1995).
- D. A. Buchanan, A. D. Marwick, D. J. DiMaria, and L. Dori, J. Appl. Phys. 76, 3595 (1994).
- D. J. DiMaria and J. W. Stasiak, J. Appl. Phys. 65, 2342 (1989).
- R. Ludeke and H. J. Wen, Appl. Phys. Lett. 71, 3123 (1997).
- 28. H. J. Wen and R. Ludeke, J. Vac. Sci. Technol. B 15, 1080 (1997).
- H. J. Wen, R. Ludeke, D. M. Newns, and S. X. Lo, *J. Vac. Sci. Technol. A* 15, 784 (1997).
- D. A. Buchanan, D. J. DiMaria, C.-A. Chang, and Y. Taur, *Appl. Phys. Lett.* 65, 1820 (1994).
- 31. H. J. Wen and R. Ludeke, J. Vac. Sci. Technol. A 16, 1735 (1998).
- 32. D. J. Dumin, J. R. Maddux, R. S. Scott, and R. Subramoniam, *IEEE Trans. Electron Devices* **41**, 1570 (1994).
- 33. K. F. Schuegraf, D. Park, and C. Hu, *Proceedings of the IEEE International Electron Devices Meeting*, 1994, p. 609. Similar results have been reported in [34].
- 34. D. J. DiMaria and J. H. Stathis, *Appl. Phys. Lett.* **71**, 3230 (1997).
- J. D. Jackson, Classical Electrodynamics, John Wiley, New York, 1961.
- P. A. Serena, J. M. Soler, and N. Garcia, *Phys. Rev. B* 34, 6767 (1986).
- S. Sze, *Physics of Semiconductor Devices*, 2nd Ed., Wiley, New York, 1981.
- H. J. Wen, R. Ludeke, D. M. Newns, S. X. Lo, and E. Cartier, *Appl. Surf. Sci.* 123/124, 418 (1998).
- P. M. Solomon and D. J. DiMaria, J. Appl. Phys. 52, 5867 (1981), and references to prior work therein.
- M. V. Fischetti, S. E. Laux, and E. Crabbé, J. Appl. Phys. 78, 1058 (1995), and references therein.
- 41. J. Maserjian, J. Vac. Sci. Technol. 11, 996 (1974).
- S. Zafar, K. Conrad, Q. Liu, E. A. Irene, G. Hames, R. Kuehn, and J. J. Wortman, *Appl. Phys. Lett.* 67, 1031 (1995).
- H. J. Wen, R. Ludeke, and A. Schenk, J. Vac. Sci. Technol. B 16, 2296 (1998); Appl. Phys. Lett. 73, 1221 (1998).
- B. Kaczer, H.-J. Im, and J. P. Pelz, J. Vac. Sci. Technol. B 16, 2302 (1998).
- Y.-N. Xu and W. Y. Ching, Phys. Rev. B 44, 11048 (1991), and references therein.
- R. Ludeke and A. Schenk, J. Vac. Sci. Technol. B 17, 1823 (1999).
- J. Maserjian and G. P. Petersson, *Appl. Phys. Lett.* 25, 50 (1974).
- M. V. Fischetti, D. J. DiMaria, L. Dori, J. Batey, E. Tierney, and J. Stasiak, *Phys. Rev. B* 35, 4044 (1987).
- J. C. Poler, K. K. McKay, and E. A. Irene, J. Vac. Sci. Technol. B 12, 88 (1994).
- S. Zafar, Q. Liu, and E. A. Irene, J. Vac. Sci. Technol. A 13, 47 (1995).
- H. S. Momose, M. Ono, T. Yoshitomi, T. Ohguru, S. Nakamura, M. Saito, and H. Iwai, *IEEE Trans. Electron Devices* 45, 1233 (1996).
- 52. K. H. Gundlach, Solid State Electron. 9, 949 (1966).
- D. A. Buchanan, F. R. McFeely, and J. J. Yurkas, *Appl. Phys. Lett.* 73, 1676 (1998).
- R. Ludeke, E. Cartier, and A. Schenk, *Appl. Phys. Lett.* 75, 1407 (1999).
- F. Bassani and G. Pastori Parravicini, Electronic States and Optical Transitions in Solids, Pergamon Press, New York, 1975.

A. Schenk and G. Heiser, *J. Appl. Phys.* 81, 7900 (1997).
 J. R. Chelikowsky and M. Schlüter, *Phys. Rev. B* 15, 4020 (1977).

Received July 9, 1999; accepted for publication December 14, 1999 Rudolf Ludeke IBM Research Division, Thomas J. Watson Research Center, P.O. Box 218, Yorktown Heights, New York 10598 (ludeke@us.ibm.com). Dr. Ludeke is a Research Staff Member in the Physical Sciences Department of the Semiconductor Sciences and Technology Department at the Thomas J. Watson Research Center. His current research interests include the atomic-scale properties of microelectronic materials, interfaces, and device structures characterized by scanning probe microscopies/spectroscopies. He received a B.S. degree in electrical engineering from the University of Cincinnati in 1961, and M.S. and Ph.D. degrees in applied physics from Harvard University in 1962 and 1968, respectively. Dr. Ludeke joined the IBM Thomas J. Watson Research Center in 1968. His areas of research have spanned a variety of subjects and included the optical properties of semiconductor thin films, molecular beam epitaxy, and characterization of III-V and II-VI semiconductor films, quantum wells, and superlattices, of which he is a co-inventor, the physics of the formation of Schottky barriers, and their characterization by synchrotron excited photoemission and scanning tunneling microscopy. Dr. Ludeke was an Alexander von Humboldt Fellow at the Max-Planck-Institute for Solid State Physics in Stuttgart, Germany, in 1977. He is a Fellow of the American Physical Society and a member of the American Vacuum Society; he is currently on the Governing Board of the American Institute of Physics.